Alexander Neifert

Brown Graduate School

Department of Molecular Pharmacology, Physiology & Biotechnology

Gold Nanorod-Mediated Near-Infrared Stimulation of Neurons in Retinal Explants

Advisor: Professor Jonghwan Lee

Committee Members:

Professor Shawna Cutting

Professor Jacquelyn Schell

May 2020

AUTHORIZATION TO LEND AND REPRODUCE THESIS

As the sole author of this thesis, I authorize Brown University to lend it to other institutions or individuals for the purpose of scholarly research.

Date: _____ Signature: _____

Alexander Neifert, Author

I further authorize Brown University to reproduce this thesis by photocopying or other means, in total or in part, at the request of other institutions or individuals for the purpose of scholarly research.

Date:_____ Signature: _____

Alexander Neifert, Author

This thesis by Alexander Neifert is accepted in its present form by the Department of Molecular Pharmacology, Physiology, and Biotechnology as satisfying the thesis requirements for the degree of Master of Science

Date: _____ Signature: _____

Dr. Jonghwan Lee, Advisor

Date: _____ Signature: _____

Dr. Shawna Cutting, Reader

Date: _____ Signature: _____

Dr. Jacquelyn Schell, Reader

Approved by the Graduate Council

Date: _____ Signature: _____

Dean of the Graduate School

Preface and Acknowledgments:

I would especially like to thank Professor Jonghwan Lee and all the members of the Lee Laboratory for their collaboration, inspiration and support thought my time at Brown University. My work would also not have been possible without the support of my family, Professor Jacquelyn Schell and Professor Shawna Cutting.

I would also like to acknowledge:

Professor Vicki Colvin

Dr. Kyungsik Eom

Dr. Taeseok Yang

Jarui Nei

Collin Polucha

Hafithe AlGhosain

Gaia Gerbaka

Carli Langevin

Collin Polucha

Oren Lederberg

Table of Contents

List of Tables and Illustrations

Abstract of *Gold Nanorod-Mediated Near-Infrared Stimulation of Neurons in Retinal Explants* by Alexander Neifert, ScM., Brown University, May 2020.

Vision loss and blindness continue to be leading causes of disability both nationally and globally. There has been progress in treating certain causes of blindness, such as uncontrolled diabetes and cataracts. However, retinal degenerative diseases such as age-related macular degeneration, retinitis pigmentosa, and Stargardt disease remain incurable. These diseases are unique in that primary cell loss occurs at the photoreceptor level, while underlying networks of bipolar, horizontal, amacrine and retinal ganglion cells generally survive. This remaining cell network provides a unique opportunity to restore vision through retinal prosthetic devices. Early electrode-based retinal prostheses have demonstrated the feasibility of this approach but have been limited in their resolution.

The Lee Laboratory has been working to develop an alternative approach, which uses near-infrared light to stimulate gold nanoparticles adjacent to retinal ganglion cells. Such an approach has the potential to achieve a much higher resolution than current electrode methods. When compared to optogenetics-based approaches, the nanoparticle stimulation does not need to genetically alter cells through viral vectors.

This thesis describes *ex vivo* studies of the promising approach. We used genetically engineered calcium indicators for clear visualization of retinal ganglion cell response. Initial investigation focused on identifying ideal voltage and pulse durations for stimulation. Improvements in perfusion and image analysis were undertaken to reduce movement artifact. Additional modifications were made to investigate the feasibility of a widefield of view so that pattern-based multicellular stimulations would be possible moving forward.

Chapter 1: Introduction

1.1 Light's Path from Cornea to Retina

The underlying anatomy and physiological processes in functional vision provide a framework when considering approaches to restoring vision. The human eye is able to process electromagnetic radiation with wavelengths ranging from approximately 300 to 700 nm. This is what forms the visual spectrum. Variations of wavelength along this spectrum define the color which is perceived. Electromagnetic radiation outside this spectrum is also present in the environment; however, it is not detected visually. Infrared and ultraviolet are the closest neighbors to the visual spectrum with infrared being at wavelengths just beyond 700 nm and ultraviolet at wavelengths just below 300 nm. Particularly relevant to later discussion, is a subset of the infrared spectrum referred to as near-infrared. The definition of the near-infrared spectrum can vary but is generally defined as between 700-2500 nm. [1, 2]

The first anatomical structure incoming light encounters is a hardened, transparent layer called the cornea. The cornea provides the initial focusing of incoming light along with a level of structural protection to more internal structures. Once light passes through the cornea, it enters the anterior chamber. This chamber contains aqueous humor, a clear fluid which aids in providing structure. A circular opening called the pupil acts to adjust how much light continues on depending on the brightness of the environment. It then reaches the lens, which is actively manipulated by ciliary muscles and serves to further focus the light on the retina. From the lens, the light continues through the vitreous humor, which composes the posterior chamber, before reaching the retina (see **Figure 1**).

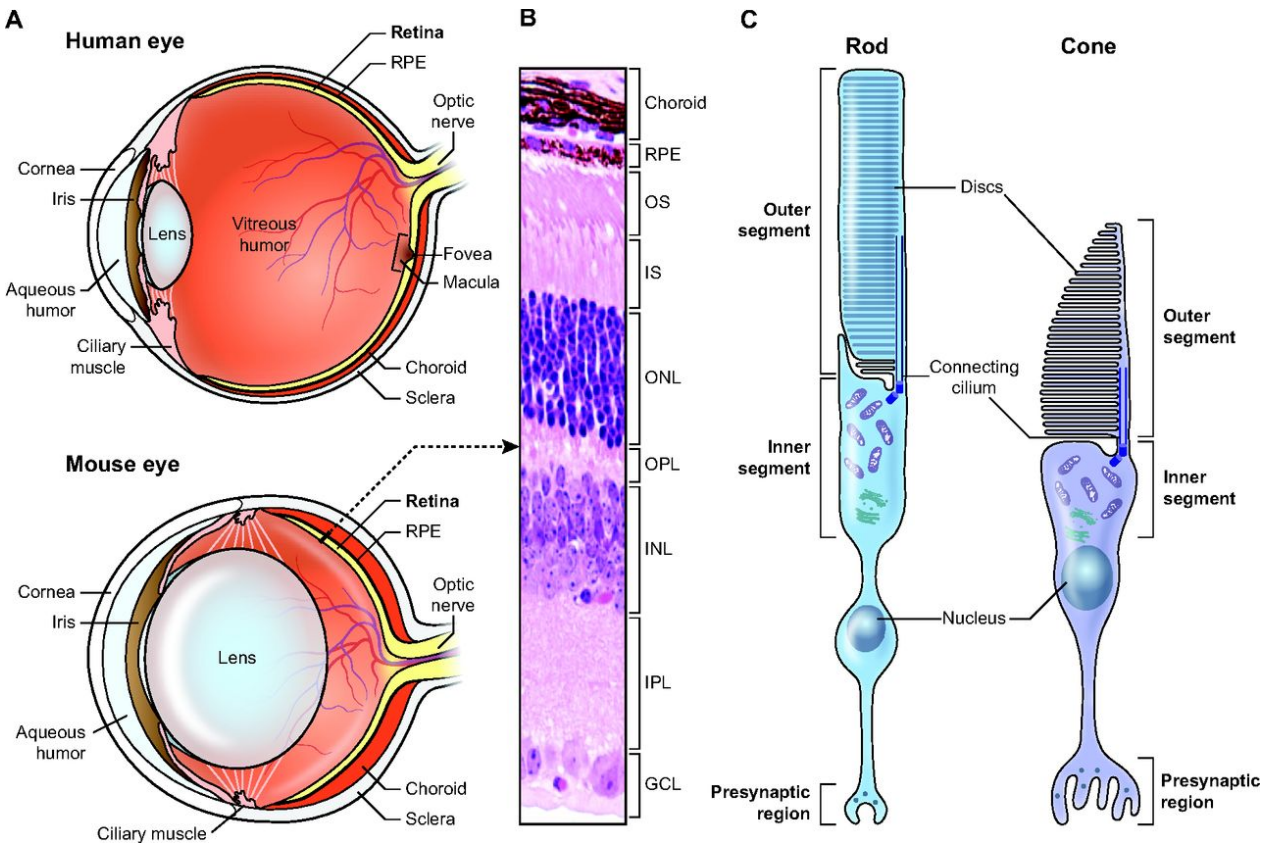

Figure 1 *Comparison of mouse and human eye along with retinal anatomy* ***1A)*** *General anatomy of mouse and human eye. Note the absence of the macula and increased lens size in mice.* ***1B)*** *Layers of the mouse retina which are comparable to those in humans.* From posterior to anterior: ***Choroid***, ***RPE****: retinal pigmented epithelium* ***OS****: outer segment of photoreceptors* ***IS****: inner segment of photoreceptors* ***ONL****: outer nuclear layer containing phoropter cell bodies* ***OPL****: outer and inner plexiform layers a synaptic region* ***INL:*** *inner nuclear layer which contains amacrine, bipolar and horizontal neurons* ***IPL****: inner plexiform layers a synaptic region* ***GCL****: ganglion cell layer which contains retinal ganglion cells.* ***1C)*** *Overview of photoreceptor morphology Adapted from Veleri et al*[3]

1.2 The Retina

The structure of the retina can seem a bit counterintuitive on initial exposure. Light must first penetrate through the cellular network of the retina before reaching the photoreceptors where it is detected. Photoreceptors consist of two distinct cell types, rods and cones (see **Figure 1C**). Cones are classified into three distinct categories by their opsins, which determine which wavelength of light is detected. L cones detect long wavelengths translating it to the color red. M cones detect middle wavelengths or the color green. S cones detect short wavelengths or the color blue. Notably, primates are the only mammals with trichromy, the ability to detect three distinct colors.[4] In mice, cones represent only 3% of photoreceptors with the majority of cones co-expressing S and M opsins.[5] Cones are estimated to make up around 5% of photoreceptors in humans, with a sharp increase in their density at and around the fovea. This concentration of cones at the fovea provides the retina with an area of particularly high visual acuity.[6]

Just as the path of light through the retina can be counterintuitive, so can the process through which photoreceptors report light detection. Photoreceptors are active at rest, releasing glutamate. Photon absorption leads to decreased activity and in turn a decrease in the release of glutamate. Bipolar cells receive glutamic stimulation from photoreceptors. For mice, cones synapse with at least nine types of bipolar cells. However, more recent findings suggest there may be up to 15 distinct types of bipolar cells.[7] One crucial role bipolar cells play, is distinguishing when light is present and absent. These are referred to as On and Off bipolar cells. Interestingly, bipolar cells synapse at unique depths of the inner plexiform layer, with ON bipolar cells synapsing closer to the ganglion cell layer (see **Figure 1B**). [8,7] A cone is typically

connected to at least 10 bipolar cells, though some unique pathways exist. S cones in the fovea of primates are unique in that they synapse in a 1:1 ratio. [9] ON bipolar cells rely upon a metabotropic glutamate receptor type 6 (mGluR6) to invert the incoming glutamate signal and cause the cell to hyperpolarize. OFF bipolar cells express an ionotropic α-amino-3-hydroxy-5-methyl-4-isoxazolepropionic acid (AMPA) and kainite glutamate receptors. High levels of glutamate released by a photoreceptor, when it has not absorbed a photon, cause depolarization of the OFF bipolar cell. The bipolar layer appears to play a key role in the rapid attenuation of incoming signals to preserve vision in settings of fluctuating light intensity. [10]

Rods are located alongside cones in the outer nuclear layer and are best known for their ability to detect a single photon (see **Figure 1**). This level of sensitivity allows for vision in low light settings and is made possible by a complex pathway with built-in amplification. The crucial first step is the absorption of a photon, which leads to isomerization of a *cis*-retinal chromophore of rhodopsin to an all-*trans* isomer. The activation of a single rhodopsin will activate 16 transducer proteins, amplifying the signal, and leading to a decrease in internal calcium. This decrease in calcium leads to a decreased release of glutamate from the rod. [11]

Currently, there is believed to be several pathways through which a rod's signal may travel. In all of these pathways, amacrine cells serve a crucial summative role between rods. Unlike cones, only one type of rod specific bipolar cell has been identified in mammals. The rod ON bipolar cell differs from cone bipolar cells in that it relies upon an amacrine cell to transmit its signal to retinal ganglion cells. Alternative pathways for ON rod transmission are constructed through direct communication with cones. Rods also serve a role in OFF pathways. These

pathways do not use a rod specific bipolar cells, but instead rely on cones, amacrine cells and cone OFF bipolar cells to reach ganglion cell layers.[11]

Horizontal cells are found in the outer plexiform layer adjacent to photoreceptors (see **Figure 1B**). They have a close relationship with bipolar cells forming ribbon synapses at the spherical ends of rods.[12] Horizontal cells are generally divided into three subtypes, with the primary distinguishing characteristic being the presence or absence of axons. Horizontal cells are thought to play a role in signal summation between photoreceptors. This is believed to create contrast enhancement and an increased ability to distinguish colors. [13]

Retinal ganglion cells (RGCs) form the ganglion cell layer and are the final point of visual stimuli processing prior to conductance down the optic nerve to the cortex (see **Figure 1B**). Serving as a higher level of visual processing, studies report a range of up to 30 functional types of RGCs in mice. These subtypes allow for information such as color, direction, orientation, edge detection, motion and frequency to be encoded prior to the signal leaving the eye.[13] There is a significant variation between mouse and human retinal ganglion cell populations. Midget or P Ganglion cells represent 70-80% of RGCs in humans, while being absent in mice and other non-humanoids. Highly concentrated around the macula, their 1:1 connections with select cones allow for the high visual acuity in this region.[11] In mice, the most prevalent type of retinal ganglion cell is the W3 cell. These appear to serve a role in identify small objects moving against a stationary background and are thought to be potentially advantageous in spotting predatory birds.[14]

1.3 Epidemiology of Blindness

The most recent estimate from the World Health Organization places the global number of blind individuals at 39 million. The Center for Disease Control reports blindness as among the top 10 disabling diseases in the United States.[15] The underlying cause of blindness varies greatly by global region. Preventable causes such as diabetes and premature birth are relatively rare in the United States but remain prevalent in some regions of the globe.[16] Differences in the underlying pathologies of blindness can have clear implications in the opportunity for targeting devices and therapeutics. Retinal degenerative disease is a broad category of currently untreatable blindness caused by either the loss or degeneration of photoreceptors. It encapsulates pathologies ranging from genetic mutations to multifactorial diseases such as age-related macular degeneration (AMD) as outlined in **Table 1**.[17] AMD is among the most common causes of blindness in the United States and is the most prevalent irreversible cause for adults over 50 (see **Table 2**)**.** Current estimates are that over 170 million people suffer from AMD, making it the third leading cause of visual impairment globally.[18]

Retinal degeneration can also occur secondary to inherited genetic diseases. The most common inheritable cause of retinal degeneration is retinitis pigmentosa, a disease with a non-syndromic prevalence of 1 in 4,000 births. Stargardt disease, also represents a significant disease burden with an estimated prevalence of up to 1 in 8,000 individuals.[19] The survival of bipolar and retinal ganglion cells in these diseases provides a unique pathway to target for restoring vision through prosthesis. As these retinal degenerative diseases represent a significant proportion of potential patients, their underlying pathology and available treatments will be explored more thoroughly in the following sections.

Phenotype (disease)	Cell type affected	Mode of inheritance	Genes
Non-syndromic monogenic			
CSNB	Rods more than cones (largely non-progressive)	Dominant	*GNAT1*, *PDE6B*, *RHO*
		Recessive	*GNAT1*, *CABP4*, *GRK1*, *SAG*
		X-linked	*CACNA1F*
LCA	Rods and cones	Dominant	*CRX*
		Recessive	*CRX*, *AIPL1*, *TULP1*, *CABP4*, *RPE65*, *CEP290*
RP	Rods more than cones and/or RPE (progressive)	Dominant	*CRX*, *NRL*, *NR2E3*, *PRPH2*, *RHO*, *ROM1*, *RPE65*
		Recessive	*ABCA4*, *MERTK*, *NRL*, *NR2E3*, *PDE6A*, *PDE6B*, *RHO*, *RPE65*, *SAG*, *TULP1*
		X-linked	*RPGR*, *RP2*
CD-CRD	Cones more than rods	Dominant	*AIPL1*, *CRX*, *PRPH2*
		Recessive	*ABCA4*, *CNGB3*, *RAB28*,
		X-linked	*CACNA1F*, *RPGR*
Macular degeneration	Rods and cones	Dominant	*PRPH2*, *ELOV4*
		Recessive	*ABCA4*
		X-linked	*RPGR*
Synaptic diseases	Rods and cones	Dominant	*UNC119*, *RIMS1*
		Recessive	*CACNA2D4*
		X-linked	*CACNA1F*, *XLRS*
Syndromic			
BBS	Rods and cones	Recessive	*BBS2*, *BBS4*, *BBS6*, *CEP290*
Joubert syndrome	Rods and cones	Recessive	*CEP290*
Senior-Loken syndrome	Rods and cones	Recessive	*CEP290*
Usher syndrome	Rods and cones	Recessive	*MYO7A*, *USH2A*

Table 1 *Monogenic inheritable causes of retinal degeneration. Adapted from Veleri et al* [17]

	Current Estimates (in millions)	2020 Projections (in millions)
Advanced Age-Related Macular Degeneration (With Associated Vision Loss)	1.8*	2.9
Glaucoma	2.2	3.3
Diabetic Retinopathy	4.1	7.2
Cataract	20.5	30.1

** Another 7.3 million people are at substantial risk for vision loss from AMD.*
Source: National Eye Institute. *Archives of Ophthalmology*. 122(4):444-676.
Available from URL: *http://www.nei.nih.gov/eyedata/pbd_tables.asp.*

Table 2 *Leading causes of blindness in the United state in 2010 and predicted in 2020. Adapted from the Center for Disease Control (CDC)*[15]

1.4 Age-related Macular Degeneration

AMD is often subdivided into “wet” and “dry”. Dry is a reference to the accumulation of lipid-rich proteins between Bruch’s membrane and the retinal pigmented epithelium. These deposits are referred to as drusens and gradually accumulate around the macula leading to

progressive vision loss. “Wet” refers to abnormal vessel growth from the choroid into regions below the retinal pigmented epithelium (RPE) as seen in **Figure 2**. Though these neovascular cases are less common, vision loss is more rapid and severe.[18] The underlying mechanism of this neovascular form of AMD is not fully understood. However, it is thought that drusen deposits lead to local hypoxia triggering the release angiogenic factors such as vascular endothelial growth factor (VEGF).[20]

Through drusen deposits are the most common diagnostic hallmark of AMD they can be found in other diseases.[21] In AMD it appears that photoreceptors and the RPE are the primary contributors to these lipid accumulations.[22] Components found within drusen plaques have led some researchers to compare these aggregations to atherosclerotic plaques and even amyloid accumulation in Alzheimer’s. Arguments have been made that these deposits are not causative but instead represent a byproduct of normal aging. Other research points to an immune response, such as the complement cascade, as being the underlying driving force in AMD.[23]

Current therapies have been more successful in targeting wet AMD through inhibiting neovascularization. Primary therapies rely on anti-VEGF medications and photodynamic treatments in which a laser is used to activate dyes. Activation of these dyes produces free radicals which lead to the occlusion of new vessels. Management of dry AMD has focused on reducing risk factors for progression, such as smoking, light exposure and inflammation. There has been some evidence that antioxidant supplements such as vitamin C and zinc oxide may slightly delay progression. Currently, there are ongoing trials to see if doxycycline may be beneficial.[24] There have also been efforts to utilize monoclonal antibodies to curb

inflammation. However, two recent phase III trials, Chroma and Spectri, failed to show efficacy.[25]

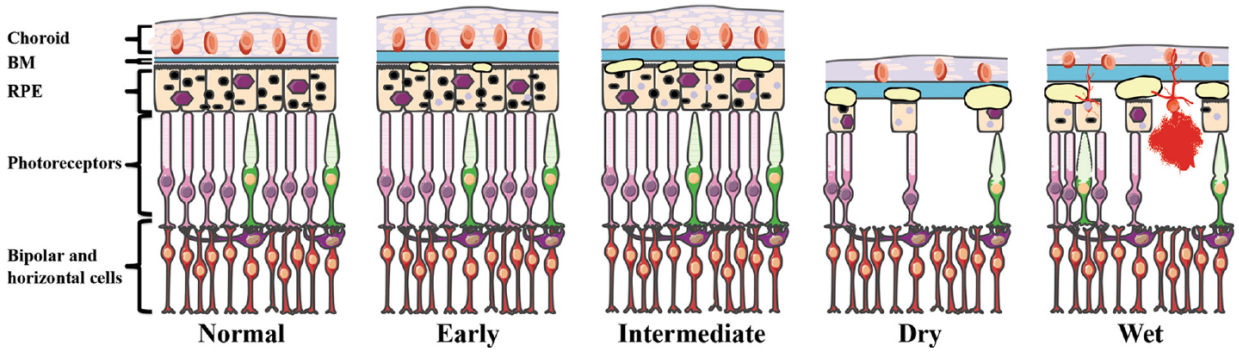

Figure 2 *Age-related macular degeneration (AMD) illustrated in a figure adapted from Tan et al. AMD leaves retinal layers beyond the photoreceptors relatively intact.*[23]

1.5 Stargardt Disease

Similar to AMD, Stargardt disease primarily impacts the macular region of the retina. It is an autosomal recessive disorder with a broad range of phenotypes. Disease progression depends on the type of *ABCA4* gene mutation and can vary significantly between individuals. Onset is typically in childhood, but can occur throughout adulthood with some patients not experiencing symptoms until their 70s.[26] The *ABCA4* gene is a member of the ATP-biding cassette transporter family. It serves to transport retinoids to the RPE from rods and cones as part of the retinoid cycle (see **Figure 3**). This allows for the removal of all-trans-retinal from the photoreceptors. Failure to clear these vitamin A byproducts leads to the formation of clumps called lipofuscin.[27] There are currently no treatments for Stargardt disease and recommendations are targeted at slowing progression. Suggested steps to slow lipofuscin

accumulation include wearing sunglasses and hats when outdoors, avoiding smoking and avoiding vitamin A supplements.[28]

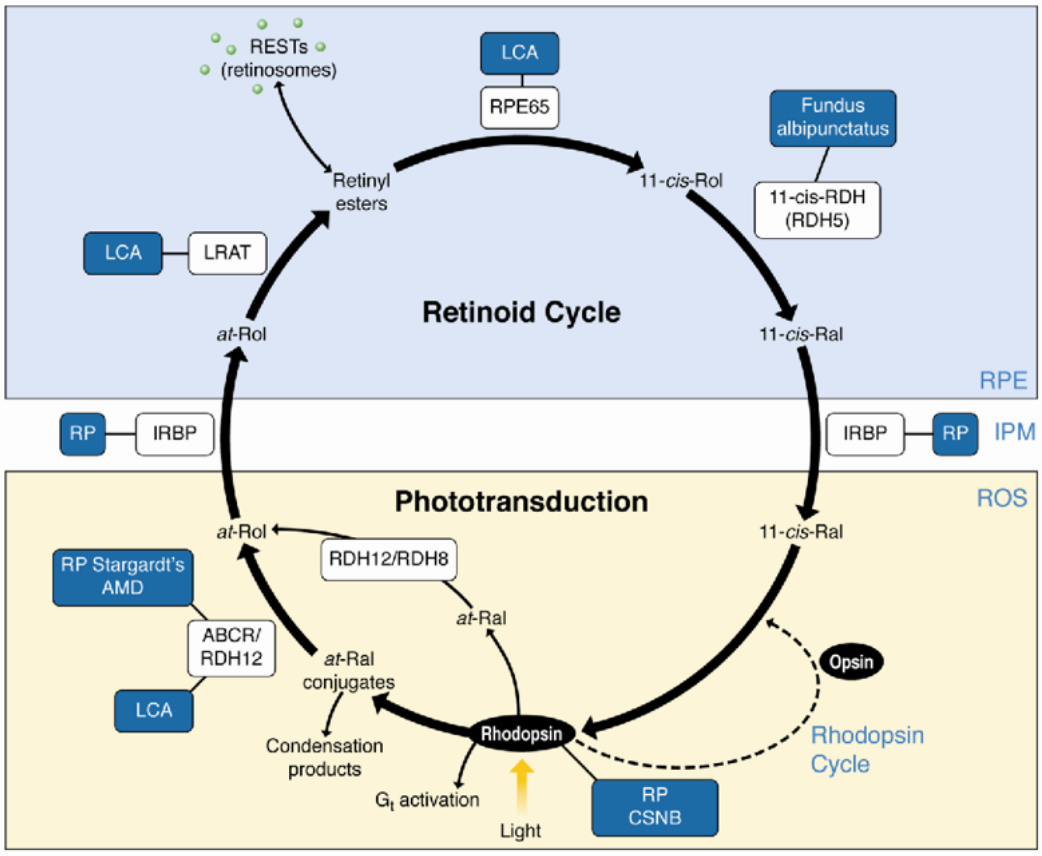

Figure 3 *Diagram outlining the pathway of the retinoid cycle. Failure along this pathway can lead to multiple diseases including Stargardts Disease. Adapted from Kiser et al*[29]

1.6 Retinitis Pigmentosa

Retinitis pigmentosa (RP) is characterized by visible pigment deposits and includes a broad range of isolated mutations and associated syndromes. RP representing a collection of over 45 genetic mutations each with a unique pathophysiology. Depending on the mutation, inheritance can be autosomal dominant, autosomal recessive and X-linked. Despite the broad range of genetic causes, the phenotypes remain similar. There is typically widespread loss of

photoreceptors due to apoptosis. Rods are typically found to be more vulnerable than cones.[19] Two processes these mutations are commonly thought to inhibit are protein folding and protein transportation. This can lead to oxidative stress and eventual photoreceptor apoptosis.[27] Some researchers suggest certain mutations such as the Rpe65 genetic defect may lead to an alternative cell death through a calcium depletion process following light stimulation.[30] There can be some loss of both inner nuclear and ganglion cells in RP. Notably, bipolar and retinal ganglion cell survival seems to be highest around the macula.[31]

Recently, there have been several new therapies introduced for RP. Prior therapies, such as vitamin A palmitate, had served only to delay progression of RP. Stem cell therapies are now being used to increase brain-derived neurotrophic factor and ciliary neurotrophic factor. Both factors appear to aid in photoreceptor and retinal ganglion cell survival. New gene therapies have also allowed for the targeting of specific defects such as the *RPGR* gene which is often mutated in X-linked RP. Additional gene therapies are being studied to improve phagocytic function through the expression of the *MERTK* gene. Other gene therapies are being used to increase glial cell-derived neurotrophic factor which also appears to increase photoreceptor survival.[32]

1.7 Mouse Models of Ocular Disease

There have been significant developments in the ability to model various ocular pathologies in mice. Since mice lack maculae, it is particularly challenging to identify appropriate models for diseases such as AMD and Stargardt. Additionally, rodents appear to not be prone to lipid accumulations on the apical RPE suggesting their transport mechanism may differ from

humans. Only simian primates have been found to accumulate drusen in a manner similar to that seen in AMD.[33] Retinitis Pigmentosa is generally thought to be more readily reproducible in mice with a variety of models available for various genetic mutations.[34,35] In **Figure 4** *Veleri et al* provides an excellent side by side comparison of a mouse model with an *rd1* mutation to a human subject with retinitis pigmentosa. Fundus photography show similar macular changes while ERG and OCT results suggest comparable microscopic and physiological changes.

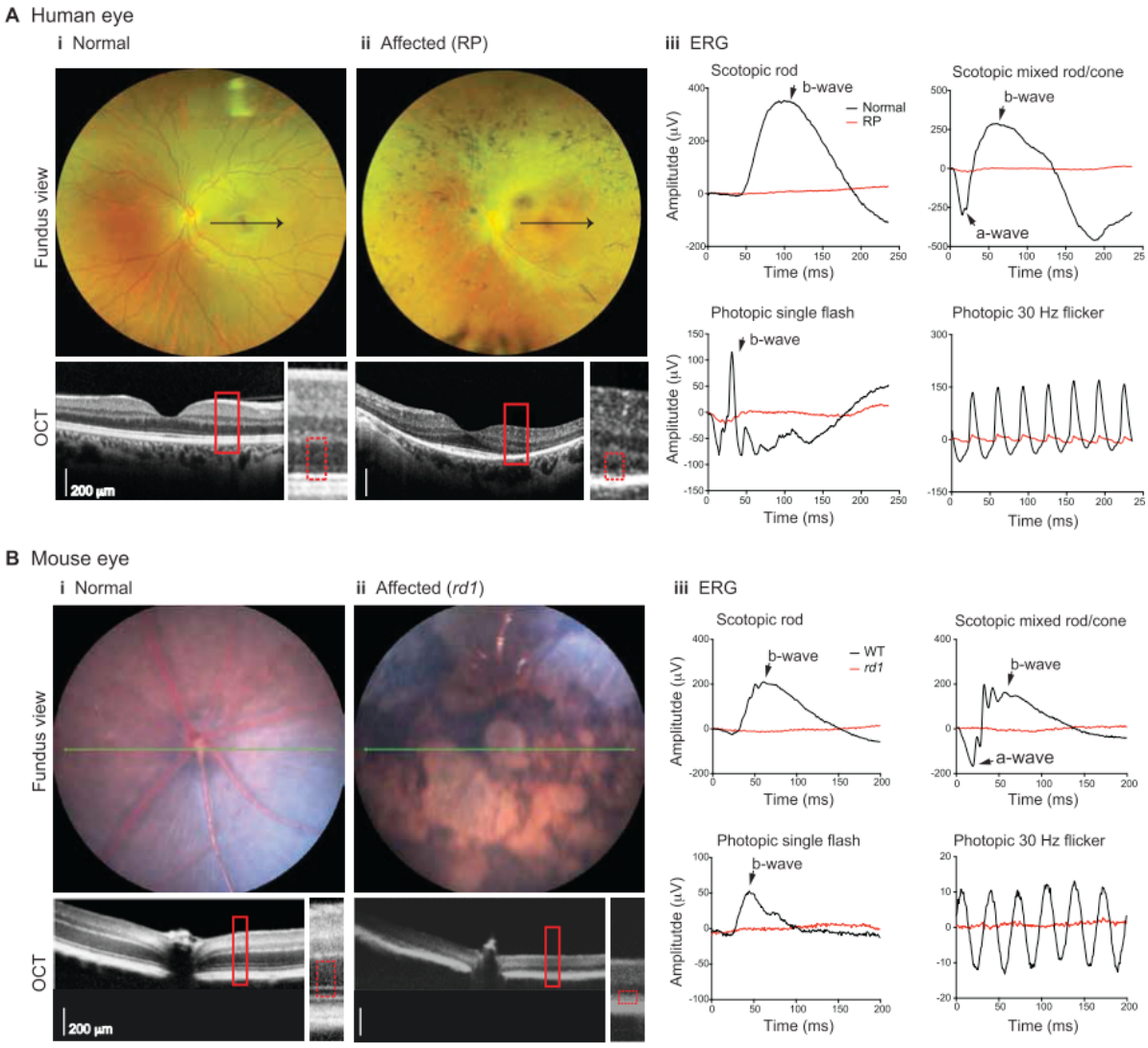

Figure 4 *Mouse retina with rd1 mutation compared to a human with retinitis pigmentosa. Clear similarities are seen, especially on OCT and ERG. Adapted from Veleri et al* [3]

Chapter 2: Rationale

2.1 Current Retinal Prosthesis

To date there have been several clinical trials involving retinal prothesis. Arguably, the earliest successful attempts at a visual prosthesis was in 1976 when a blind subject was able to read brail produced through cortical stimulation. More recently, devices such as the Argus II have had successful trials that showed both quantitative and self-reported improvements in vision. This device was approved by the FDA in 2013 and relies upon an externally mounted camera which transmits to an epiretinal 60-electrode array. Other devices, such as the Alpha IMS, have used subretinal electrodes for stimulation.[36] Alpha AMS, an improved version of the IMS, was able to achieve the highest reported visual acuity to date at 20/546 with a 1,600 pixel implant.[37] However, most other implants consist of less than 100 pixels which is far less than the 600- 1000 pixels believed to be needed in order to produce meaningful improvement. [38,39]

Interestingly, electrode array densities are likely to be constrained not by the manufacturing challenges, but issues of current conductance within the *in vivo* environment. Findings by *Behrend et al* suggest that the minimum attainable spatial resolution of electrodes is likely to be close to 150 µm. They estimate this would limit the highest attainable visual acuity to around 20/660.[40] Alpha AMS has already reported performance close to this suggested limit, but its best performance up to 20/546 is still within the legal blindness (20/200). Ongoing developments in viral vectors and gene therapy have brought the prospect of optogenetic approaches to retinal prosthesis. Yet challenges still remain in cell selection, image processing, and the use of viral vectors in human subjects. [41]

2.2 Infrared Stimulation

Optical approaches using a focused beam would address the resolution issue. Infrared (IR) stimulation had shown clear benefits in its ability to produce higher spatial resolution stimulation while remaining contact free. Neural stimulation is typically achieved with a local cellular temperature changes of a fraction to a few degrees.[42] However, water readily absorbs wavelengths in the IR spectrum making transmission through tissue or fluid filled spaces problematic. Undesired IR absorption can lead to damaging heat and has the potential to alter multiple cell signaling pathways.[43]

2.3 Overview of Near Infrared Stimulation

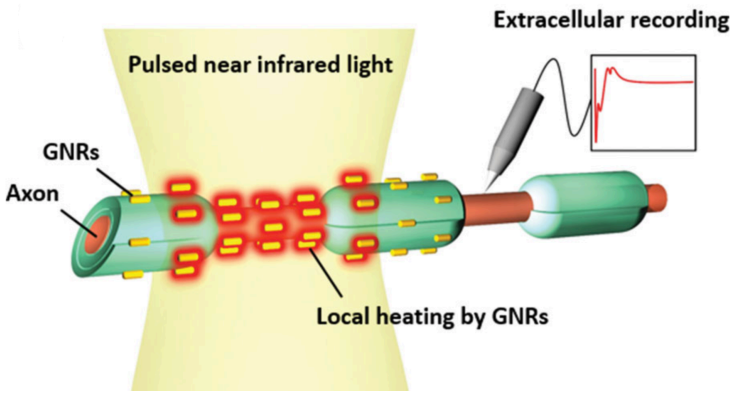

Figure 5 *Conceptual illustration of NIR excitation of AuNRs to stimulate the sciatic nerve. Adapted from Eom et al*[44]

The near infrared spectrum is generally considered to be from around 750 to 2500 nm[2] The shortened wavelength relative to the infrared spectrum allows for transmission through water and tissue with minimal absorption. The lack of absorption decreases the risk of

undesired bulk tissue heating and cellular modulation. Prior studies by *Eom et al* had demonstrated the ability of gold nanorods (AuNRs) to increase the photothermal effect of infrared beams (see **Figure 5**). AuNR generated highly localized increases in temperature which in turn induce action potentials at lower stimulation thresholds. This process is generally referred to as localized surface plasmon resonance (LSPR). *Eom et al* then proceeded to demonstrate the feasibility of neuronal stimulation using wavelengths in the near infrared spectrum combined with gold nanorods (see **Figure 6**). [44–46]

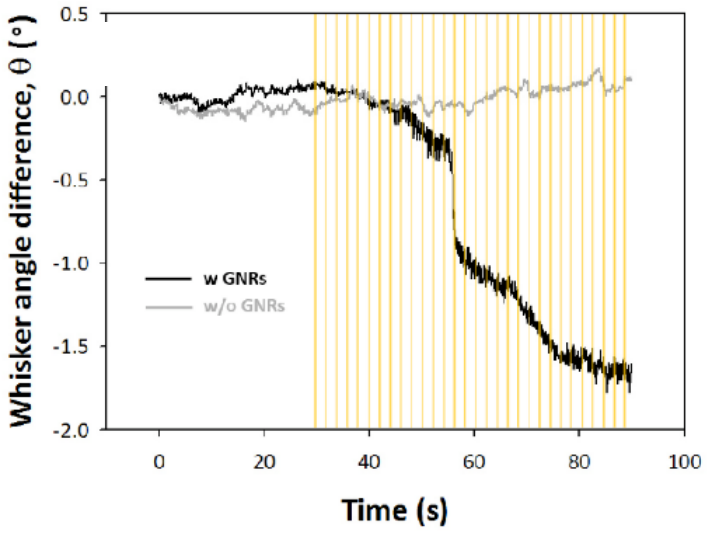

Figure 6 *Experimental results from Eom et al demonstrating effective stimulation of the rat vibrissae motor cortex using gold nanorods (GNRs) and NIR. Yellow lines represent stimulation points, black line represents stimulations with GNRs and the gray line represents without GNRs.*[45]

Principals of localized surface plasmon resonance (LSPR) are crucial to the successful application of AuNRs. In order for a LSPR to occur the nanoparticle must be metallic and small

enough that characteristics of the nanoparticle's electrons behaviors begin to be predictably constrained by the nanoparticle's dimensions. These electrons can then be excited with light of a larger wavelength than the nanoparticles dimension. When LSPRs occur in AuNRs aggregated adjacent to a cell, it leads to highly localized heating. AuNRs of 5 nm and 25 nm used in the following experiments conveniently absorb in the NIR range. This allows for wavelengths to be used that provide good tissue penetration, while avoiding wavelengths that interact with water, and may lead to off target heat generation. [47] The region of lowest absorption for NIR in biological tissues appears to be between 600-1200 nm.[48] Between 650-900nm may be even more ideal as it further avoids minimal thermal interactions with blood and water.[49]

Localized heat produced by LSPRs is thought to stimulate neurons through two processes, though the exact mechanisms have not yet been fully elucidated. One proposal, described by *Shapiro et al,* is that localized heat alters electrical capacitance of the plasma membrane. These capacitance changes appear to be completely reversible and are likely generalizable to many cell types. [50,44] The vanilloid transient receptor ion channel (TRPV1) has also been identified as a cation channel which opens in response to temperature change. It has a notably higher affinity to calcium, 10:1, over sodium.[51,44] These TRPV1 channels have been documented to be present and play a key role in regulating RGC activity(see **Figure 7**).[52]

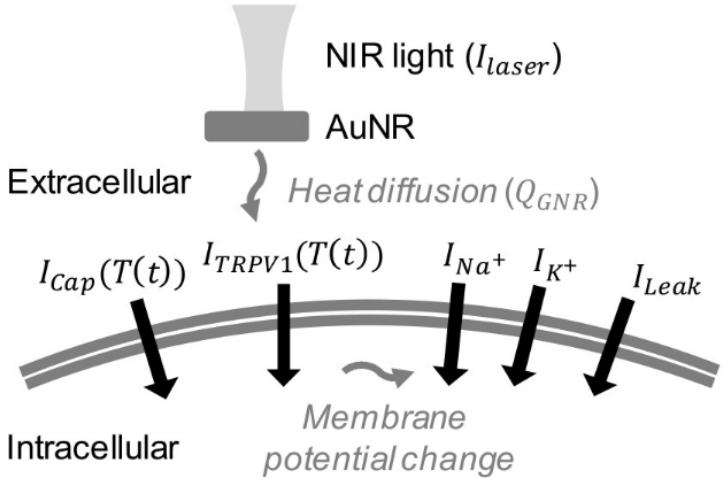

Figure 7 *Diagram of potential mechanism through which near infrared stimulation of AuNRs may lead to a membrane potential change. Adapted from Eom et al* [53]

2.4 Gold Nanorod Delivery to Retina

In transitioning these finding to the retina, it was important to consider approaches for delivering AuNRs. Several methods of current retinal therapeutic delivery were identified as potentially applicable. All of these approaches rely on microneedles and are categorized based on where the therapeutic is delivered. Most common are intravitreal, subretinal and suprachoroidal delivery (see **Figure 8**). For these studies an intravitreal (IVT) approach was used due to its broad clinical use, documented safety, ease in repeatability, and potential for broader dispersion along the retina.[54]

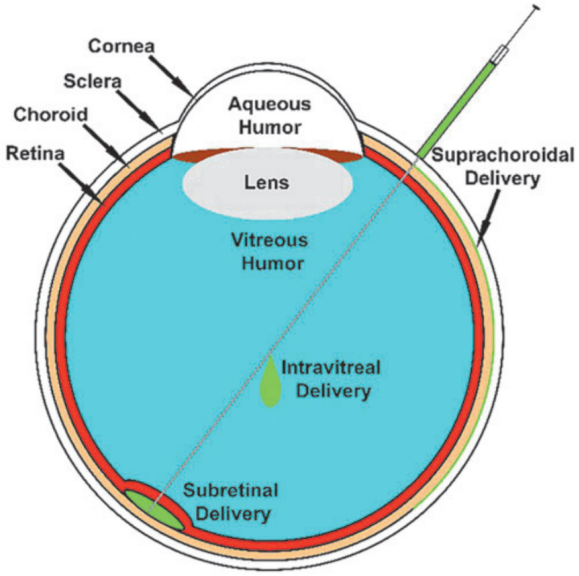

Figure 8 *Illustration of three methods for therapeutic delivery to the retina. Adapted from Hartman et al*[55]

One of the challenges faced when using an intravitreal approach to therapy delivery is the internal limiting membrane (ILM). This extracellular matrix composed of at least 10 distinct proteins had proven to be a barrier in prior studies.[56,57] Fortunately, several enzymes have shown efficacy in creating pores within the ILM to allow for improved delivery. Two enzymes that seem particularly successful in breaking own the ILM are heparinase III and hyaluronan lyase. Prior studies with these enzymes had not shown any long term effects on retinal function at 12 month follow up in mice.[54] Several studies were conducted by colleagues within the Lee Laboratory to demonstrate that AuNRs could be delivered to RGCs through intravitreal injections. They were able to verify penetration and distribution of AuNRs among retinal ganglion cells using both two-photon luminescence (TPL) and scanning electron microscope (SEM) imaging.

2.5 Genetically Encoded Calcium Indicators

In order to track retinal ganglion cell activity mice lines were selected that expressed the genetically encoded calcium indicator green fluorescent protein-calmodulin fusion protein (GCaMP3). For ex vivo experiments transgenic mice with GCaMP3 promoted under the thymus cell antigen promoter (Thy-1) gene were selected. Thy-1 had been previously documented as driving GCaMP expression in multiple neuronal cell populations including nearly 100% of retinal ganglion cells. [58] GCaMP relies upon an energy transfer between two light sensitive molecules called a Förster resonance energy transfer.[59] Junichi Nakai is credited with creating GCaMP through combining calmodulin, a myosin light chain and a circularly permutated green fluorescent protein. This structure causes increased calcium concentrations to induce a detectable conformational change (see **Figure 9**).[59] There have since been multiple iterations of the protein with GCaMP3 being one of the more established.[60] GCaMP responses can vary significantly depending on the cell, stimulus, expression level and other factors. In light evoked responses of transfected retinal ganglion cells, GCaMP3 had a half rise of approximately 200ms and a half decay of 710ms.[60] Generally, a peak in fluorescence is produced around 1 second and gradually fades over 4-6 seconds. [61,62]

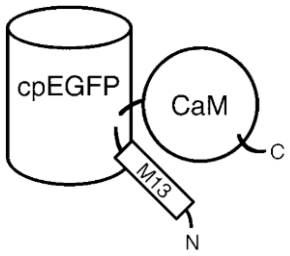

Figure 9 *Diagram of original Green fluorescent protein calmodulin fusion protein. Figure Adapted from Nakai et al* [63]

2.6 Objectives of Thesis

This thesis will serve to document the transition from a 40x to a 20x *ex vivo* imaging platform for monitoring gold nanorod-mediated near-infrared stimulation of retinal ganglion cells. Initial work focused on analyzing prior 40x imaging data to identify necessary steps to more accurately capture GCaMP responses following stimulation. Motion artifact was identified early on as a major challenge to reliable *ex vivo* imaging. The thesis will outline steps taken in modifying both experimental setup and image analysis to address potential artifact. Additional experiments where conducted at 20x magnification to ensure clear cell visualization, test NIR stimulation parameters and retinal ganglion cell response. These experiments will aid in building a reliable imagining platform for conducting experiments to identify ideal gold-nanorod delivery approaches, gold-nanorod characteristics, and allow for future multicellular stimulation experiments.

Chapter 3: Methods

3.1 Subjects

Animal experiments were conducted under Brown University's Institutional Animal Care and Use Committee (IACUC) guidance and supervision. Animals were housed in temperature and humidity-controlled rooms on 12-hour light/dark cycles. All animals were allowed unlimited access to food and water. Transgenic mice expressing GCaMP3 on Thy1 were purchased from The Jackson Laboratory (Bar Harbor, Maine, USA) item B6.Cg-Tg(Thy1-GCaMP3)6Gfng/J). Prior research by *Blandford et al* had confirmed near 100% expression of GCaMP3 in the retinal

ganglion cell population with this promoter.[64] These hemizygous mice were bred with wild type C57BL/6J mice also purchased from The Jackson Laboratory to establish a colony. Genotyping was performed by real-time PCR (Transnetxy, Cordova, Tennessee USA) and allowed for identification of GCaMP3 positive pups.

3.2 Synaptic Blockers

Synaptic blockers were used to prevent potentially damaging excitation from blue light (469 nm) exposure during *ex vivo* imaging. This bright blue light was required to visualize fluorescence changes in GCaMP3 positive RGCs. Synaptic blockers were added to a 200ml of AMES and used to perfuse the imaging well for five minutes prior to the blue light being turned on. The imaging perfusion medium consisted of the following molar concentrations 3.33×10^{-5} mol/L 6-Cyano-7-nitroquinoxaline-2,3-dione disodium salt hydrate (CNQX) (MillporeSigma) was used to inhibit AMPA/kainate receptors. 3.00×10^{-5} mol/L of D(−)-2-Amino-5-phosphonopentanoic acid (AP5) (MillporeSigma) was used to inhibit NMDA receptors on RGCs. 1.00×10^{-5} mol/L of L-(+)-2-Amino-4-phosphonobutyric acid (L-APB) (MillporeSigma) was used to further prevent overstimulation by inhibiting the agonist mGluR6 which is found on both rod and cone bipolar cells. [65,66]

3.3 Gold Nanorod and Enzyme Preparation

Solutions containing AuNRs of 25 nm and 5 nm diameter were created using AuNRs purchased from Nanopartz (Salt Lake City, Utah, USA). AuNRs were conjugated with streptavidin, an adaptor molecule which can be used as the basis for various bioconjugation

approaches. [67] No additional conjugations were performed in these experiments but are currently being investigated. Ames medium was used to dilute to the desired concentration. A combination of two enzymes were used to aid in gold nanorod penetration through the ILM**.** Heparinase III solution and 20 µl Hyaluronan lyase were buffered in Tris-HCl + BSA + Ca buffer for a final concentration of 0.125Su per 5 µl based on prior findings by *Cehajic-Kapetanovic et al*.[54]

3.4 Gold Nanorod delivery

Mice were anesthetized using isoflurane. Proper anesthetization was verified after five minutes and a mydriatic solution was applied. A gentle massage was performed followed by artificial tears 2 minutes later. Whiskers were trimmed to avoid contamination and artificial tears were applied throughout the procedure. A microliter syringe was prepared with 0.5 µl of AuNRs, 0.5 µl of enzyme and 0.5 µl of Ames medium. The upper lid was retracted with a cotton applicator. Forceps were used to apply gentle force to slightly protrude and stabilize the eye. A 26G needle was used to create a small puncture at the limbus. The microliter syringe was then inserted at a 45-degree angle and advanced into the vitreous prior to intravitreal delivery. Delivery was performed by lab colleague Jiarui Nie.

3.5 Retinal Dissection

Prior to dissection Ames medium was prepared using guidelines outlines by MilllporeSigma (Burlington, Massachusetts, USA). Sodium bicarbonate and a constant perfusion 5% CO2 where used to equilibrate to medium to physiological pH. Mice were then euthanized

using CO_2 exposure at a rate of 0.2 ml/min for 5 minutes. Manual external stimuli was applied to hind leg to ensure no withdrawal response. Once euthanasia was confirmed cervical dislocation was performed. Forceps were then used to enucleate the eyes and place them in a perfused Ames medium. Dissection was then conducted in a petri dish under red light with constant perfusion using a dissecting microscope (Olympus, Shinjuku, Tokyo, Japan). The eye was stabilized by gripping extraocular muscles at their insertion with forceps. A 20-gauge needle was used to pierce the eye at the limbus (corneal-scleral intersection) allowing for insertion of dissecting scissors. A hemisection was then continued along the limbus, releasing the cornea and exposing the anterior chamber. Gentle pressure was applied to the sclera just anterior to the optic nerve with one forceps while grasping and retrieving the lens with the other. Once the lens was removed, areas of separation between the pigmented epithelium and retina were identified. Forceps were inserted in parallel at the site of separation, and opposing force was exerted to induce a tear in the sclera. This process was repeated while ensuring not to damage the retina.

Once the retina had been fully isolated four orthogonal cuts were made allowing the retina to flatten from its natural cup shape as outlined in **Figure 10**. The retina was then placed with the anterior side up on filter paper dampened with Ames medium. Rapidly, a layer of mesh was used to secure the retina to the filter paper and then secure it to the slide using silicone adhesive. Once the retina was secured to the slide, active perfusion was resumed.

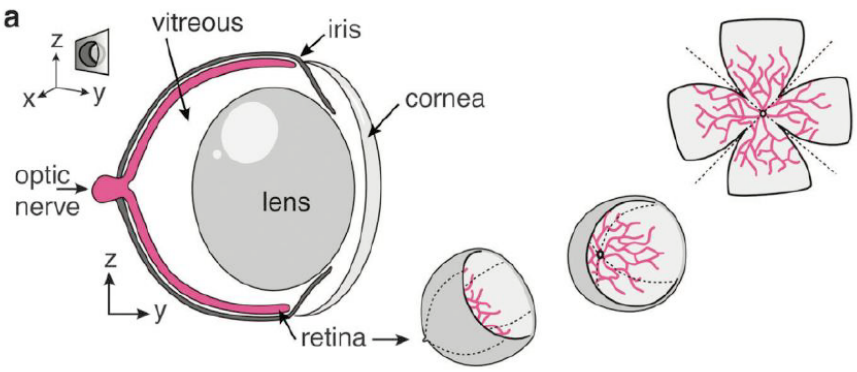

Figure 10 *Illustration of octagonal cuts to generate a flattened retina for imaging. Adapted from Milde et al.*[68]

3.6 Experimental Setup

Once the retina was mounted in the live cell imaging chamber, it was placed on the platform and transitioned to a heated perfusion system. A flask containing 200 ml of AMES medium along with synaptic blockers as described above was perfused using a rate flow regulator (B.Braun Medical Inc, Bethlehem, PA, USA). The perfusion was run at 2.5 ml/min through an in line heater (Warner Instrument, Hamden CT, USA). Temperature was monitored using a in well sensor wire attached with putty. The heating element was adjusted to maintain a well temperature of 30 +/-2 °C (see **Figure 11**). Suction was matched to the perfusion rate to allow for a steady turnover of well medium. Suction tip was kept slightly above the well's top edge to promote smooth flow. Blue light at approximately 469 nm was used to visualize florescence of GCaMP3 positive RGCs. Slide position was adjusted manually to allow for clear visualization and targeting of individual cells.

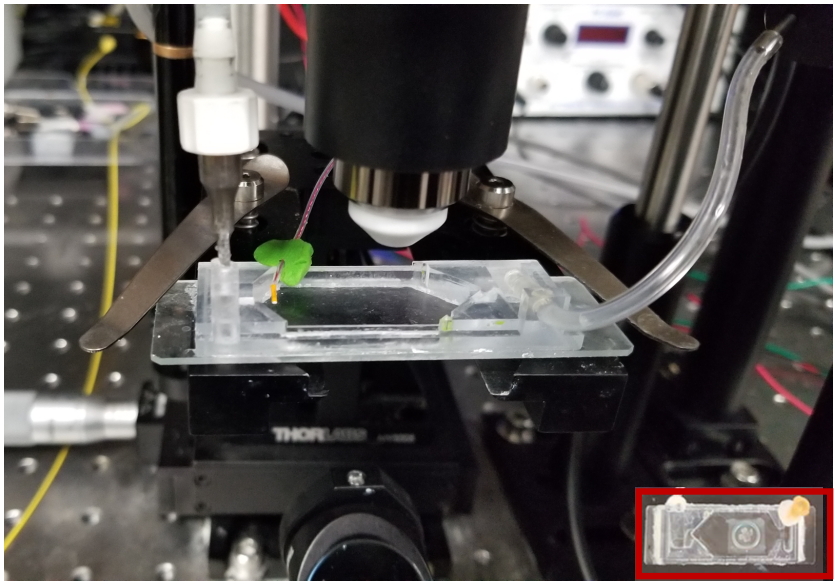

Figure 11 *Overview of experimental setup for 20X ex vivo. Green putty on left is for temperature probe attachment. Suction is on left and inflow from heating element is on right. Red insert is overhead shot of mounted retina in perfusion well.*

3.7 Data Acquisition

Cells were brought into focus while monitoring image data being acquired through a graphical user interface developed within LabView (National Instruments, Austin Texas). Prior to beginning imaging stimulation, filters were removed, gain was reduced to 0 and blue light was reduced to a minimum and a metal target was put on the platform. The NIR beam was then visualized and focused to a circle on an with an approximate diameter of 20 µm. A target box was created in LabView around the point of focus to allow for cell selection for stimulation (see **Figure 12**). Prior to imaging filters were placed to eliminate laser artifact and blue light was increased to maximum intensity. Cells were then brought into focus and an individual RGC was centered in the target box. Stimulation parameters adjusted between trials were laser voltage

and pulse duration. The following remained consistent across trials: Exposure: 100 ms, Gain 30 dB Frame time 100.32 ms. Laser off time was the time between pulses and was kept at 100.0 ms. Pulse number is the number of stimulation for every laser test, which was kept at 10. Rest times between pulses were kept at 2 seconds before the first stimulation and 7 seconds after each of the following stimulations (see **Figure 13**).

Once the program was running, on screen monitors of intensity and stimulations where cleared prior to beginning capture periods. During a trial, 10 NIR laser pulse sequences were triggered manually using the test laser button and could only be reinitiated after 7 seconds. One monitor provided live feedback on the overall field intensity (blue tracing in **Figure** 12). Another monitor showed intensity in the region of interest, as defined by the box around the point of NIR laser stimulation (ROI white box in field of view on left, intensity red tracing on right **Figure 12**). Stimulation signal was also tracked (green tracing in **Figure 12**). Each trial's data was saved under a unique name indicating both the voltage and pulse duration. Typically, a cell underwent 10 stimulations composed of 10 pulses for 100 pulses total.

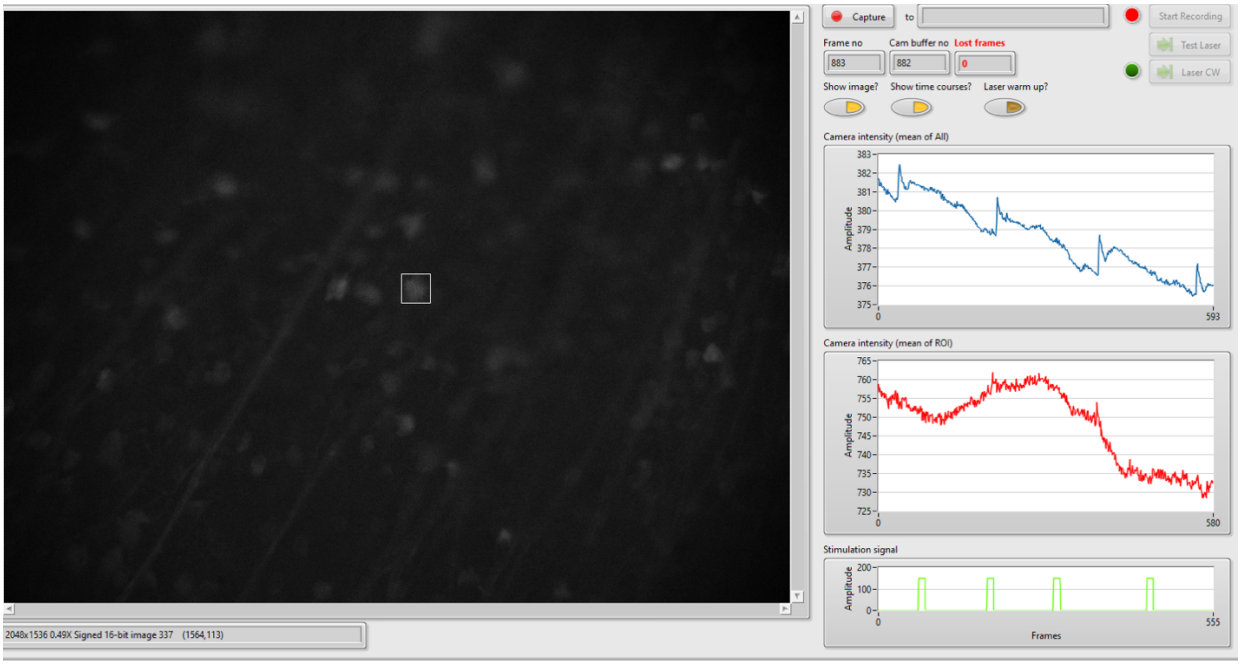

Figure 12 *Graphical user interface of LabView imaging acquisition software. Field of view on left with cells visible as hyperintensities. White rectangle outlines ROI which is the area where the NIR laser was visualized prior to the experiment. Blue tracing upper right reports overall fluorescence. Red tracing records fluorescence within the ROI*

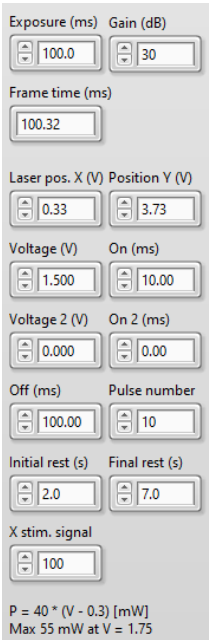

Figure 13 *Overview of experimental parameters available within LabView control panel for imaging data acquisition. Voltage and the On duration where the only variables adjusted between trials.*

3.8 Data Analysis

Image data was processed in a MATLAB (MathWorks, Natick, Massachusetts, USA) based image analysis program. This code was written by Professor Jonghwan Lee. Files were selected from the shared data server using a distinct user ID, experiment ID and data ID. Processed data was then stored with its own unique ID. Stimulation points were automatically identified when possible. In some instances, automatic identification failed and stimulation points were identified through manual selection.

The data was then filtered using a spatial median filter with a 2D kernel of dimensions 3 x 3 to reduce random noise. This was followed by a Gaussian filter with a standard deviation of 1 to reduce stochastic noise (See **Figure 14**)

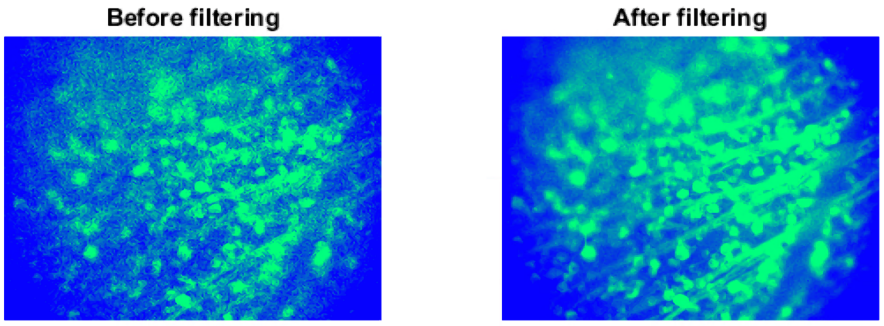

Figure 14 *Sample image pre and post median and Gaussian filtering acquired during 20x experiments.*

Following filtering, motion corrections were made using on an algorithm to minimize the mean square error (MSE) of the images. This was done by making the setting p1.oREG equal to 1. If the data set extended beyond 5 minutes, there was no improvement in correlation

p1.oREG was set to 2. A setting of 2 allowed for manual adjustments in the maximum movement by pixels allowed in both X and Y (see **Figure 15**).

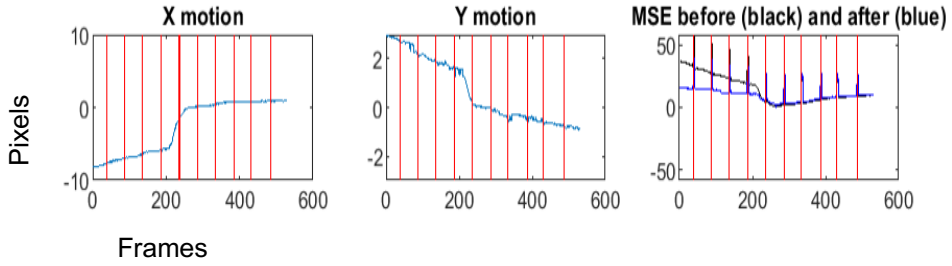

Figure 15 *Results of motion correction performed by in house MATLAB program. Y axis is in pixels X axis is in frames. MSE represents mean square error.*

The data was then sliced and averaged in reference to stimulation points. The resulting data was displayed as an average image at a given time point from stimulation. Time points were selected typically from -1 second before stimulation to a maximum of six seconds following stimulation. Images representing averaged dF/F results for time points prior to and after stimulation were then viewed in series. Images that captured artifact from the laser during stimulation were excluded from analysis (see **Figure 16**).

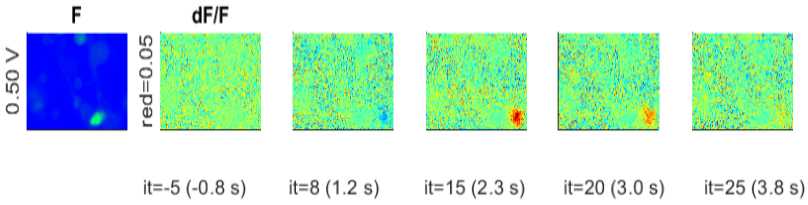

Figure 16 *Image analysis showing averaged dF/F. Red and blue represent increases and decreases in dF/F respectively. Green is representative of no significant change.*

Chapter 4: Results

4.1 40x Magnification Experiment Results

Initial image analysis was conducted on images obtained previously by Gaia Gerbaka, a colleague with the Lee Laboratory. This magnification had the benefit of revealing AuNR clusters on the cell which could be specifically targeted by a narrow NIR beam for stimulation. Although the strategy of visualizing and targeting AuNR clusters is not applicable to the in vivo and clinical environment, the strategy was useful in the initial ex vivo study.

Below are several examples of early imaging and analysis. One of the goals in these experiments was to identify stimulation parameters that produced the strongest and most consistent response. Conversely, we also wanted to identify laser power thresholds and pulse duration that potentially led to cell damage. For a given cell trials were conducted at a range of voltages driving the laser from 0.2 V to 1 V. Pulse duration was changed between cells and ranged from 0.1 ms to 10 ms. Higher voltage and longer pulse durations represent a larger energy of NIR light.

In analysis images, colors reflect average fluoresce change over multiple trials at a given time relative to stimulation. Red represents increased fluorescence and should translate to a relative increase in calcium a given time point. Blue represents a decrease in fluorescence and potentially lower calcium at a given time over. The threshold for a red indication is determined during image processing and is displayed on the vertical axis as the dF/F threshold for red. A proportional decrease in fluorescence would be represented by blue. Throughout the experiment several cells demonstrated what appeared to be a clear response to NIR stimulation (see **Figure 17**)

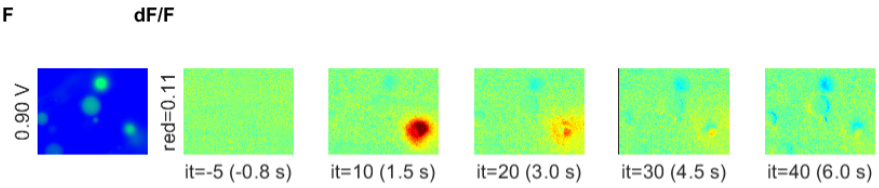

Figure 17 *A trial demonstrating a rapid increase in intracellular calcium following stimulation. Consistent with expected GCaMP3 response. Laser strength was 0.9 V (23 mW) with a pulse duration of 0.1 ms.*

However, responses were not consistent across all trials. Notably, multiple trials demonstrated what appeared to be a delayed response to stimulation (see **Figure 18**). Prior studies had reported a peak fluorescence should occur prior to 2 seconds following stimulation.[61,62] However, multiple trials had peaks appeared greater than 3 seconds following stimulation. This led to concern that we may be capturing localized movement artifact

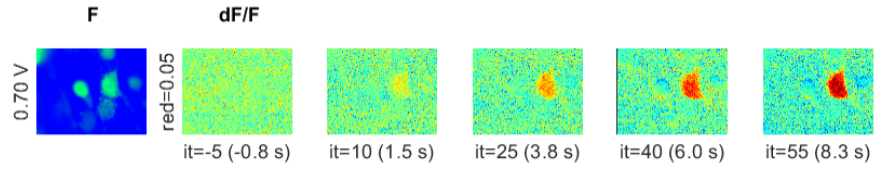

Figure 18 *A trial demonstrating a delayed increase in intracellular calcium following stimulation. Laser strength was 0.7 V (15 mW) with a pulse duration of 0.1 ms.*

Several stimulations seemed to result in potential calcium leakage. This occurred in some instances at voltages as low as 0.2 V (see **Figure 19** and **20**). Due to the inconsistent

occurrence and lack of correlation with laser voltage, there was also concern that these fluorescence changes may reflect motion artifact.

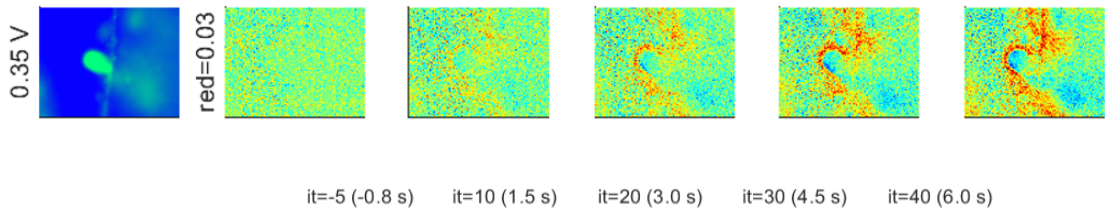

Figure 19 *A trial demonstrating a potential gradual decrease in intracellular calcium with an increase in surrounding fluorescence. This may be indicative of cellular injury with leakage to the surrounding medium. Laser strength was 0.35 V (1.5 mW) with a pulse duration of 1 ms.*

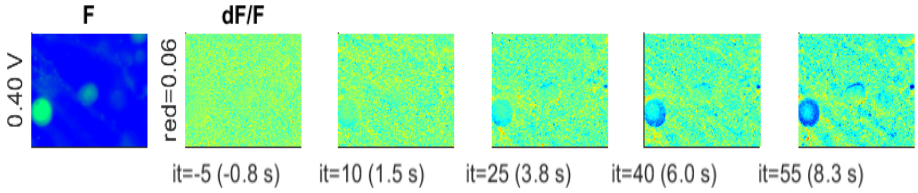

Figure 20 *A trial demonstrating a potential gradual decrease in intracellular calcium. This may be secondary to cellular injury. Laser strength was 0.4 V (3 mW) with a pulse duration of 1 ms.*

Though several images appeared to capture a clear response to optical stimulation, however this was not seen consistently and did not occur in the early trials further analyzed below. Other sequences were suggestive of potential cell injury but also occurred irregularly and did not correspond with higher voltages as expected. **Figure 21** and **22** show graphical representations of trials with either increased or decreased dF/F for targeted cells at various pulse durations and voltages. Targeted cells were the intended cell for stimulus. **Figure 21** shows the greatest number of trials with fluorescence increases were seen with 10 ms pulses.

Figure 22 failed to show any significant correlation between laser voltage and changes in fluorescence. **Figure 23** and **Figure 24** examine responses from targeted cell for stimulus alongside neighboring cells. Neighboring cells represent cells within the field of view but not intentionally targeted for stimulation. A larger number of florescence changes where noted in neighboring cells than targeted cells particularly at higher voltages and larger pulse durations.

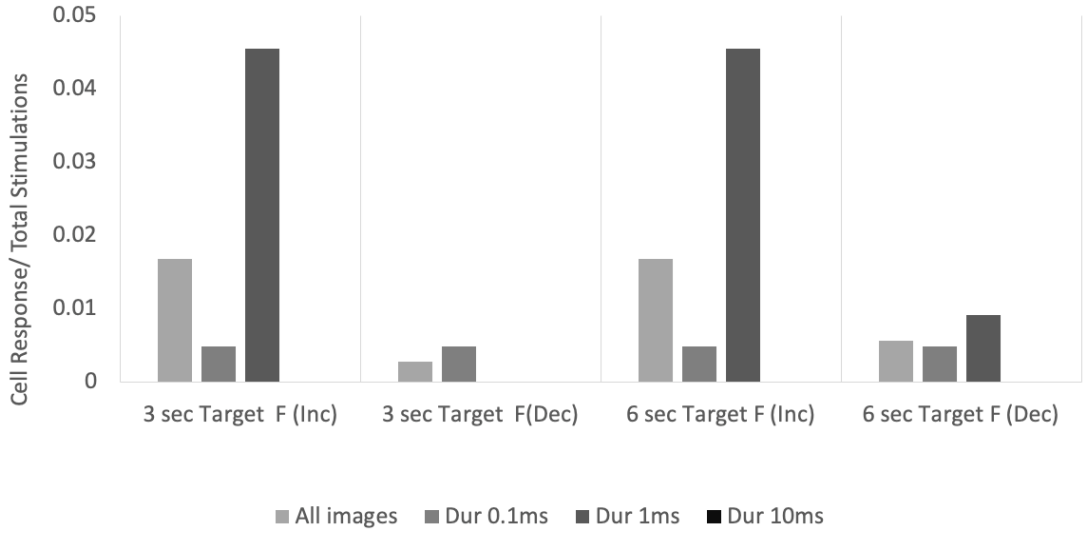

Figure 21 *Targeted cell responses following stimulation at various NIR laser pulse durations. Positive events are either increases or decreases in dF/F. Y axis represents the ratio of these positive events to the total number of images. Shade represents 0.1ms, 1ms, and 10ms laser pulse durations . Results selecting for target cell activity at 3 and 6 seconds with increase (Inc)or decreased (Dec) dF/F also denoted (X axis). No increases or decreases were visualized at the 0.8 second time window so this time frame was not included. No changes in dF/F were seen with 10ms pulse in the target cell. 1ms pulse generated the greatest number of increased dF/F, however, this occurred in less than 5 percent of images.*

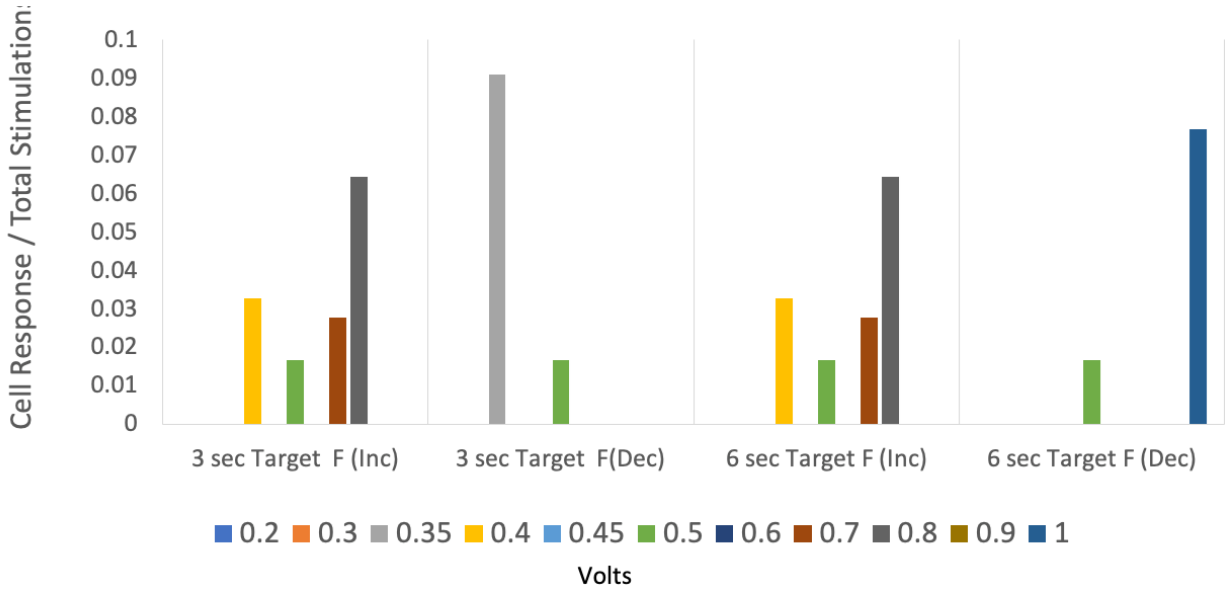

Figure 22 *Targeted cell responses following stimulation at various NIR laser voltages. Positive events are either increases or decreases in dF/F. Y axis represents the ratio of these positive events to the total number of images. Colors represents voltage in volts denoted in key. Evaluated at 3 seconds and 6 second increase (Inc)or decreased (Dec) dF/F on X axis. No events of increased or decreased dF/F were seen at 0.8 seconds so it was not included in figure.*

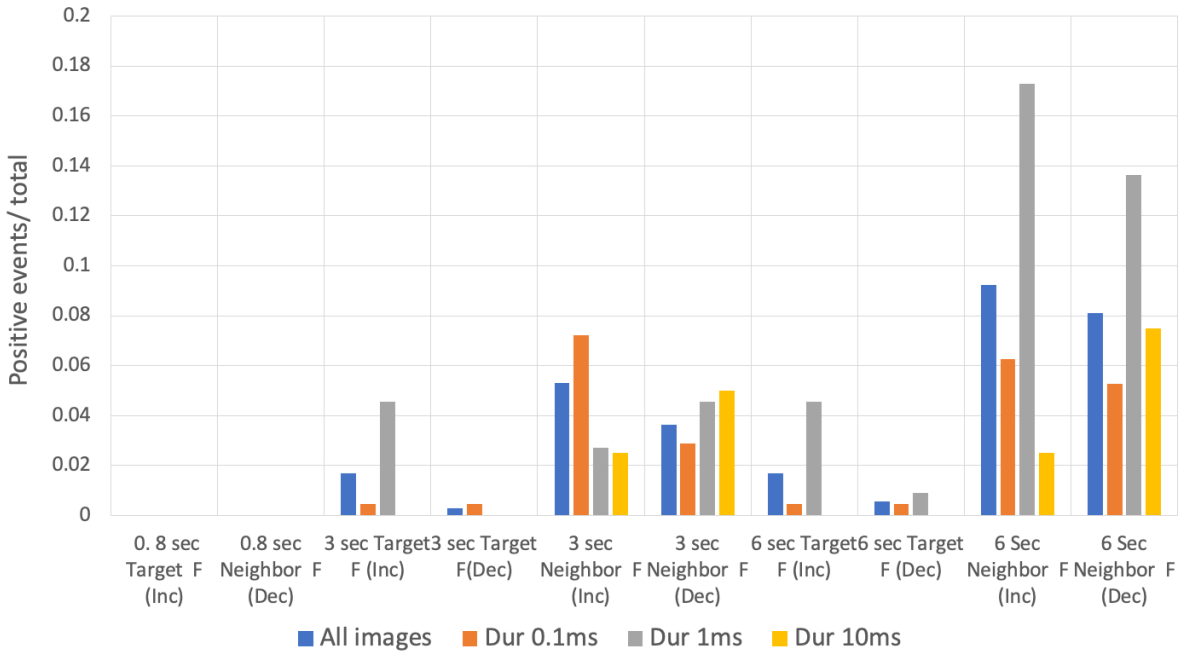

Figure 23 *Targeted and neighboring cell responses following stimulation at various NIR laser pulse durations . Positive events represent either increases or decreases in dF/F . Evaluated for 0.1ms, 1ms, and 10ms laser pulse durations (color). Y axis represents the ratio of these positive events to the total number of images. Images evaluated at 0.8 seconds, 3 seconds and 6 seconds along with increase (Inc)or decreased (Dec) dF/F also denoted (x axis). The majority of changes in F both increasing and decreasing occurred outside the target area. The target area more frequently increased in F than decreased in F when compared to the shift seen in neighboring cells. Pulse durations of 1 ms seemed to lead to the most frequent increase in dF/F at the target cells. No increases or decreases were visualized at the 0.8 second time window.*

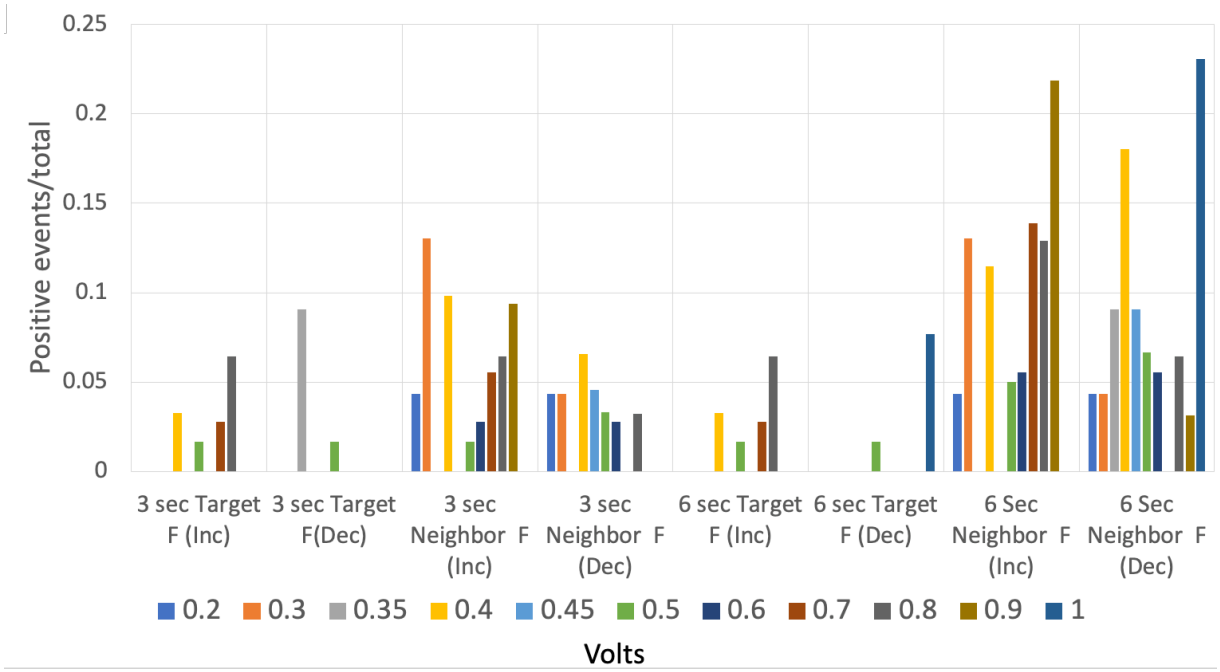

Figure 24 *Targeted and neighboring cell responses following stimulation at various NIR laser voltages. Positive events are either increases or decreases in dF/F. Y axis represents the ratio of these positive events to the total number of images. Colors represents voltage in volts denoted in key. Evaluated at 3 seconds and 6 second increase (Inc)or decreased (Dec) dF/F on X axis. No events of increased or decreased dF/F were seen at 0.8 seconds so it was not included in figure*.

Overall these initial imaging results were hard to draw any clear conclusions from and were likely limited in some part from motion artifact secondary to perfusion. Though the changes in fluorescence in neighboring cells could represent activity, the delayed response was felt to be more indicative of cell motion in the plane of focus. Limitations to these trials included a narrow beam size and visualized targeting of AuNRs, a technique that was not realistic to scale to an *in vivo* device. The minimal number of cells visible in a given field of view also limited the opportunity of investigating multicellular stimulation patterns in the future. We

were able to remove frames obscured by laser artifact, however, this artifact frequently persisted up to the 0.8 seconds following stimulation. As such, it could be partially masking changes in GCaMP fluorescence. These findings would lead to the implementation of an improved inline imaging perfusion setup and additional efforts to reduce motion artifact through updated MATLAB code.

4.2 20x Magnification Imaging

The custom fluorescent microscope was modified to allow for a widefield view at 20x magnification while still providing resolution of individual cells (see **Figure 25**)**.** The widefield of view made the imaging less susceptible to local cell motion. One new challenge encountered was the need for a particularly flat retinal explant. Uneven areas in the retina drastically limited the number of cells which could be brought in to focus at a given time under 20x. As might be expected, the higher lower magnification also failed to provide the resolution necessary to identify AuNRs clusters. Visualizing multiple cells would allow for future experimentation to include multicellular stimulation.

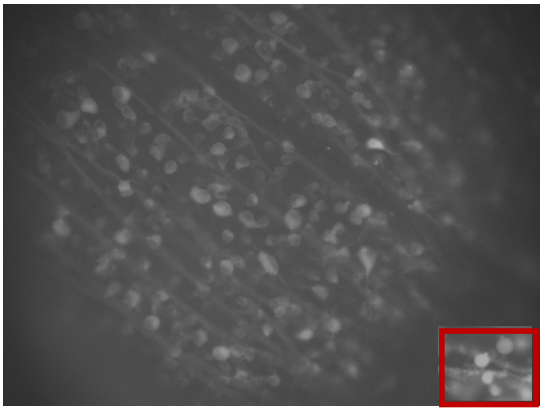

Figure 25 *40x magnification overlay on a widefield 20x image showing differences in the number of visible cells.*

Chapter 5 Conclusion

5.1 Discussion

Early analysis of *ex vivo* imaging trials lacked consistency to provide insight into ideal voltage and pulse duration parameters. Several trials appeared to show potential cell damage, in that there was decreased cell fluorescence following stimulation (see **Figure 19** and **Figure 20**). However, these findings were difficult to interpret fully. Although decreased fluorescence may represent calcium leak from cell injury, these changes could also be seen with vertical cell movements out of the plane of focus.

Target cell response following stimulation was not seen consistently in early trials. Many of the recorded fluorescence changes began beyond the 3 second window (see **Figure 23** and **Figure 24**). However, prior literature suggests a GCaMP3 peak should occur less than 2 seconds following stimulation. Additionally, more fluorescence changes were documented in neighboring cells than target cells. These findings lead to concerns that delayed fluorescence

changes likely do not reflect successful stimulation but are more likely to be motion artifacts. Motion that brings a cell into the plane of focus could potentially lead to such fluorescence changes. As only several cells are visible in any 40X image accurate determination of global motion remains slightly limited. By broadening the field of view to include multiple cells, the image analysis will be less susceptible to retinal motion in the newly developed widefield imaging system. Additional efforts to minimize fluctuations in perfusion and heating should also aid in improving imaging accuracy in future trials. Further refinement of MATLAB code to accurately detect and correct motion artifact has also begun to be implemented as described above.

Understanding the safety of AuNRs is a crucial component to further development of this technology. Multiple components are likely to contribute to a given particles potential toxicity. Alterations in the surface chemistry of AuNRs through coatings seems to have a significant impact on their biocompatibility. It also appears that the aspect ratio has minimal to no impact on biocampatability.[69] One study by *Li et al* found larger AuNRs, greater than 14nm in diameter, had lower cytotoxicity and higher clearance rates.[70]

In an *in vivo* study conducted by *Bartneck et al* mice underwent intravenous injection of AuNRs with analysis performed on various organs to see where the highest accumulations occurred. The liver was found to have the highest accumulation followed by the spleen and lung. It should be noted that these rods were stabilized with cetyltrimethylammonium bromide (CTAB). CTAB is a common chemical used in the production of AuNRs, but alternative production methods exist. AuNR conjugations with peptides also seem to directly impact macrophage response. Particular peptide sequences triggered an M1 (classically activated)

response while others produced an M2 (alternatively activated) macrophage response. Some tripeptide sequences appeared to be responsible for causing an increased Alaninie Aminotranferse (ALT) when given at a weekly dose of 12µg/ kg. ALT, which serves as a marker of liver damage, was notably unaffected by other nanorod coatings and peptide sequences. [71]

Additional factors, such as AuNR charge, also play a potential role in toxicity. There is some evidence that a positive charge and smaller particle size may lead to increased toxicity. Particles below 2 nm seems to induce chemical reactivity that does not occur with larger particles.[72] Charge is also an important factor as components of the eye such as the hyaluronic acid in the vitreous humor carry a negative charge.[73] Multiple studies have shown that negatively charged therapeutics are more successful in traversing the vitreous humor and reaching the retina. [74] Surface characteristics that allow AuNRs to directly bind to cells, make those cells more responsive to optical stimulation as well as less likely to washout.[48,75] Variations in binding may require even more specific investigation to identify toxicity risk for a given nanoparticle. Application of prior nanotoxicity studies are also limited as intravitreal injection is likely to lead to a significantly different distribution compared to intravenous administration.

5.2 Next Steps

Initial trials have shown that widefield *ex vivo* retinal imaging with single cell resolution is feasible. Initial widefield stimulation trials have also been conducted. However, the size of these data sets have presented new challenges when it comes to image analysis with prior MATLAB code and current hardware. Initial steps will focus on updating the MATLAB code to

allow for processing within the current hardware limitations. Future experiments will continue to focus on identifying procedural changes to improve consistency of single cell response to stimulation. Procedures and literature will also be reviewed to design experiments to better ensure retinal ganglion cells are healthy and responsive throughout imaging and stimulation. This will include trials to determine if increased exposure time to synaptic blockers may be necessary to prevent excessive excitation from blue light.

New mouse models have also been selected to generate progeny that undergo retinal degeneration and are transgenic for GCaMP6. These mice from The Jackson Laboratory carry the RHO^{P23H} mutation that leads to autosomal dominant RP in humans. Not only will this allow for more accurate modeling of RP, but it will also reduce the risk of injury from blue light. Additionally, GCaMP6 is an improved calcium indicator which reacts more rapidly and with greater intensity to calcium fluctuations. This will improve our ability to capture retinal ganglion cell activity. Further investigation will continue into parameters such as pulse duration, voltage and beam size as our results so far have been inconclusive. Once single cell stimulations are consistently successful, widefield imaging will allow for experiments to be conducted with various NIR stimulation patterns across multiple cells. These continued *ex vivo* experiments, alongside *in vivo* trials, will provide a promising path to better understand the capabilities of NIR based retinal prosthesis.

References

1. Bell JF. Visible and near-infrared spectroscopy (VIS-NIR). In: *Encyclopedia of Planetary Science*. Dordrecht: Springer Netherlands; 1997:911-915. doi:10.1007/1-4020-4520-4_443
2. Kaim W. Concepts for metal complex chromophores absorbing in the near infrared. *Coord Chem Rev*. 2011;255(21-22):2503-2513. doi:10.1016/J.CCR.2011.01.014
3. Veleri S, Lazar CH, Chang B, Sieving PA, Banin E, Swaroop A. Biology and therapy of inherited retinal degenerative disease: Insights from mouse models. *DMM Dis Model Mech*. 2015;8(2):109-129. doi:10.1242/dmm.017913
4. Carvalho LS, Pessoa DMA, Mountford JK, Davies WIL, Hunt DM. The genetic and evolutionary drives behind primate color vision. *Front Ecol Evol*. 2017;5(APR):1-12. doi:10.3389/fevo.2017.00034
5. Wang Y V., Weick M, Demb JB. Spectral and temporal sensitivity of cone-mediated responses in mouse retinal ganglion cells. *J Neurosci*. 2011;31(21):7670-7681. doi:10.1523/JNEUROSCI.0629-11.2011
6. Jonas JB, Schneider U, Naumann GOH. Count and density of human retinal photoreceptors. *Graefe's Arch Clin Exp Ophthalmol*. 1992;230(6):505-510. doi:10.1007/BF00181769
7. Tsukamoto Y, Omi N. Classification of mouse retinal bipolar cells: Type-specific connectivity with special reference to rod-driven AII amacrine pathways. *Front Neuroanat*. 2017;11(October):1-25. doi:10.3389/fnana.2017.00092

8. Kolb H, Ralph N, Eduardo F. The Organization of the Retina and Visual System. *Webivcson*. 2019:1-11.

9. Wässle H, Puller C, Müller F, Haverkamp S. Cone contacts, mosaics, and territories of bipolar cells in the mouse retina. *J Neurosci*. 2009;29(1):106-117. doi:10.1523/JNEUROSCI.4442-08.2009

10. Nawy S. Modulation of TRPM1 and the mGluR6 Cascade in ON Bipolar Cells. In: Martemyanov KA, Sampath AP, eds. *G Protein Signaling Mechanisms in the Retina*. New York, NY: Springer New York; 2014:99-119. doi:10.1007/978-1-4939-1218-6_7

11. Wässle H. Parallel processing in the mammalian retina. *Nat Rev Neurosci*. 2004;5(10):747-757. doi:10.1038/nrn1497

12. Nemitz L, Dedek K, Janssen-Bienhold U. Rod Bipolar Cells Require Horizontal Cells for Invagination Into the Terminals of Rod Photoreceptors. *Front Cell Neurosci*. 2019;13(September):1-12. doi:10.3389/fncel.2019.00423

13. Boije H, Fard SS, Edqvist PH, Hallböök F. Horizontal cells, the odd ones out in the retina, give insights into development and disease. *Front Neuroanat*. 2016;10(JUL):1-12. doi:10.3389/fnana.2016.00077

14. Zhang Y, Kim IJ, Sanes JR, Meister M. The most numerous ganglion cell type of the mouse retina is a selective feature detector. *Proc Natl Acad Sci U S A*. 2012;109(36):E2391-E2398. doi:10.1073/pnas.1211547109

15. CDC- Centers for Disease Control and Prevention. Burden of Vision Loss - About Vision Health - Vision Health Initiative (VHI). https://www.cdc.gov/visionhealth/basic_information/vision_loss_burden.htm. Accessed

March 4, 2020.

16. World Health Organization. *Universal Eye Health. A Global Action Plan 2014-2019*.; 2013.

17. Veleri S, Lazar CH, Chang B, Sieving PA, Banin E, Swaroop A. Biology and therapy of inherited retinal degenerative disease: Insights from mouse models. *DMM Dis Model Mech*. 2015;8(2):109-129. doi:10.1242/dmm.017913

18. Pennington KL, DeAngelis MM. Epidemiology of age-related macular degeneration (AMD): associations with cardiovascular disease phenotypes and lipid factors. *Eye Vis*. 2016;3(1):1-20. doi:10.1186/s40662-016-0063-5

19. Hamel C. Retinitis pigmentosa. *Orphanet J Rare Dis*. 2006;1(1):1-12. doi:10.1186/1750-1172-1-40

20. Stefánsson E, Geirsdóttir A, Sigurdsson H. Metabolic physiology in age related macular degeneration. *Prog Retin Eye Res*. 2011;30(1):72-80. doi:10.1016/j.preteyeres.2010.09.003

21. Abdelsalam A, Del Priore L, Zarbin MA. Drusen in Age-Related Macular Degeneration: Pathogenesis, Natural Course, and Laser Photocoagulation–Induced Regression. *Surv Ophthalmol*. 1999;44(1):1-29. doi:10.1016/S0039-6257(99)00072-7

22. Mullins RF, Russell SR, Anderson DH, Hageman GS. Drusen associated with aging and age-related macular degeneration contain proteins common to extracellular deposits associated with atherosclerosis, elastosis, amyloidosis, and dense deposit disease. *FASEB J*. 2000;14(7):835-846. https://pubmed.ncbi.nlm.nih.gov/10783137.

23. Tan PL, Bowes Rickman C, Katsanis N. AMD and the alternative complement pathway: genetics and functional implications. *Hum Genomics*. 2016;10(1):23. doi:10.1186/s40246-

016-0079-x

24. Al-Zamil WM, Yassin SA. Recent developments in age-related macular degeneration: A review. *Clin Interv Aging*. 2017;12:1313-1330. doi:10.2147/CIA.S143508

25. Holz FG, Sadda SR, Busbee B, et al. Efficacy and safety of lampalizumab for geographic atrophy due to age-related macular degeneration: Chroma and spectri phase 3 randomized clinical trials. *JAMA Ophthalmol*. 2018;136(6):666-677. doi:10.1001/jamaophthalmol.2018.1544

26. Westeneng-van Haaften SC, Boon CJF, Cremers FPM, Hoefsloot LH, den Hollander AI, Hoyng CB. Clinical and Genetic Characteristics of Late-onset Stargardt's Disease. *Ophthalmology*. 2012;119(6):1199-1210. doi:10.1016/j.ophtha.2012.01.005

27. Cideciyan A V., Aleman TS, Swider M, et al. Mutations in ABCA4 result in accumulation of lipofuscin before slowing of the retinoid cycle: A reappraisal of the human disease sequence. *Hum Mol Genet*. 2004;13(5):525-534. doi:10.1093/hmg/ddh048

28. NIH. Stargardt Disease | National Eye Institute. Eye Conditions and Diseases. https://www.nei.nih.gov/learn-about-eye-health/eye-conditions-and-diseases/stargardt-disease. Accessed March 10, 2020.

29. Kiser. *Retinoic Acid in Retina, Cycle from Palcevski*. Vol 1821.; 2013. doi:10.1016/j.bbalip.2011.03.005.Key

30. Fain GL. Why photoreceptors die (and why they don't). *BioEssays*. 2006;28(4):344-354. doi:10.1002/bies.20382

31. Loewenstein JI. Outer Retinal Degeneration. *Arch Ophthalmol*. 2004;122(4):587. doi:10.1001/archopht.122.4.587

32. Ludwig PE, Freeman SC, Janot AC. Novel stem cell and gene therapy in diabetic retinopathy, age related macular degeneration, and retinitis pigmentosa. *Int J Retin Vitr*. 2019;5(1):1-14. doi:10.1186/s40942-019-0158-y

33. Fletcher EL, Jobling AI, Greferath U, et al. Studying age-related macular degeneration using animal models. *Optom Vis Sci*. 2014;91(8):878-886. doi:10.1097/OPX.0000000000000322

34. Krebs MP, Collin GB, Hicks WL, et al. *Mouse Models of Human Ocular Disease for Translational Research*. Vol 12.; 2017. doi:10.1371/journal.pone.0183837

35. Won J, Shi LY, Hicks W, et al. Mouse Model Resources for Vision Research. *J Ophthalmol*. 2011;2011:1-12. doi:10.1155/2011/391384

36. Mills JO, Jalil A, Stanga PE. Electronic retinal implants and artificial vision: Journey and present. *Eye*. 2017;31(10):1383-1398. doi:10.1038/eye.2017.65

37. Stingl K, Schippert R, Bartz-Schmidt KU, et al. Interim results of a multicenter trial with the new electronic subretinal implant alpha AMS in 15 patients blind from inherited retinal degenerations. *Front Neurosci*. 2017;11(AUG):445. doi:10.3389/fnins.2017.00445

38. Weiland JD, Cho AK, Humayun MS. Retinal Prostheses: Current Clinical Results and Future Needs. *Ophthalmology*. 2011;118(11):2227-2237. doi:10.1016/j.ophtha.2011.08.042

39. Derrick L. Cheng DAB and PBGM. Retinal Prostheses-— Now and in the Future. *Rev Opthalmology*. June 2017. https://www.reviewofophthalmology.com/article/retinal-prostheses-now-and-in-the-future. Accessed March 4, 2020.

40. Behrend MR, Ahuja AK, Humayun MS, Chow RH, Weiland JD. Resolution of the epiretinal

prosthesis is not limited by electrode size. *IEEE Trans Neural Syst Rehabil Eng*. 2011;19(4):436-442. doi:10.1109/TNSRE.2011.2140132

41. Barrett JM, Berlinguer-Palmini R, Degenaar P. Optogenetic approaches to retinal prosthesis. *Vis Neurosci*. 2014;31(4-5):345-354. doi:10.1017/S0952523814000212

42. Chernov M, Roe AW. Infrared neural stimulation: a new stimulation tool for central nervous system applications. *Neurophotonics*. 2014;1(1):011011. doi:10.1117/1.nph.1.1.011011

43. Tsai S-R, Hamblin MR. Biological effects and medical applications of infrared radiation. *J Photochem Photobiol B Biol*. 2017;170(1):197-207. doi:10.1016/j.jphotobiol.2017.04.014

44. Eom K, Kim J, Choi JM, et al. Enhanced Infrared Neural Stimulation using Localized Surface Plasmon Resonance of Gold Nanorods. *Small*. 2014;10(19):3853-3857. doi:10.1002/smll.201400599

45. Eom K, Im C, Hwang S, et al. Synergistic combination of near-infrared irradiation and targeted gold nanoheaters for enhanced photothermal neural stimulation. *Biomed Opt Express*. 2016;7(4):1614. doi:10.1364/boe.7.001614

46. Eom K, Hwang S, Yun S, Byun KM, Jun SB, Kim SJ. Photothermal activation of astrocyte cells using localized surface plasmon resonance of gold nanorods. *J Biophotonics*. 2017;10(4):486-493. doi:10.1002/jbio.201600280

47. Petryayeva E, Krull UJ. Localized surface plasmon resonance: Nanostructures, bioassays and biosensing-A review. *Anal Chim Acta*. 2011;706(1):8-24. doi:10.1016/j.aca.2011.08.020

48. Paviolo C, Stoddart PR. Gold nanoparticles for modulating neuronal behavior.

Nanomaterials. 2017;7(4):1-14. doi:10.3390/nano7040092

49. Weissleder R. A clearer vision for in vivo imaging. *Nat Biotechnol*. 2001;19(4):316-317. doi:10.1038/86684

50. Shapiro MG, Homma K, Villarreal S, Richter CP, Bezanilla F. Infrared light excites cells by changing their electrical capacitance. *Nat Commun*. 2012;3:310-376. doi:10.1038/ncomms1742

51. Richter CP, Matic AI, Wells JD, Jansen ED, Walsh JT. Neural stimulation with optical radiation. *Laser Photonics Rev*. 2011;5(1):68-80. doi:10.1002/lpor.200900044

52. Sappington RM, Sidorova T, Ward NJ, Chakravarthy R, Ho KW, Calkins DJ. Activation of transient receptor potential vanilloid-1 (TRPV1) influences how retinal ganglion cell neurons respond to pressure-related stress. *Channels*. 2015;9(2):102-113. doi:10.1080/19336950.2015.1009272

53. Eom K, Byun KM, Jun SB, Kim SJ, Lee J. Theoretical Study on Gold-Nanorod-Enhanced Near-Infrared Neural Stimulation. *Biophys J*. 2018;115(8):1481-1497. doi:10.1016/j.bpj.2018.09.004

54. Cehajic-Kapetanovic J, Milosavljevic N, Bedford RA, Lucas RJ, Bishop PN. Efficacy and Safety of Glycosidic Enzymes for Improved Gene Delivery to the Retina following Intravitreal Injection in Mice. *Mol Ther - Methods Clin Dev*. 2018;9(June):192-202. doi:10.1016/j.omtm.2017.12.002

55. Hartman RR, Kompella UB. Intravitreal, subretinal, and suprachoroidal injections: Evolution of microneedles for drug delivery. *J Ocul Pharmacol Ther*. 2018;34(1-2):141-153. doi:10.1089/jop.2017.0121

56. Halfter W, Dong S, Dong A, Eller AW, Nischt R. Origin and turnover of ECM proteins from the inner limiting membrane and vitreous body. *Eye (Lond)*. 2008;22(10):1207—1213. doi:10.1038/eye.2008.19

57. Dalkara D, Kolstad KD, Caporale N, et al. Inner limiting membrane barriers to aav-mediated retinal transduction from the vitreous. *Mol Ther*. 2009;17(12):2096-2102. doi:10.1038/mt.2009.181

58. Blandford SN, Hooper ML, Yabana T, Chauhan BC, Baldridge WH, Farrell SRM. Retinal characterization of the thy1-GcaMP3 transgenic mouse line after optic nerve transection. *Investig Ophthalmol Vis Sci*. 2019;60(1):183-191. doi:10.1167/iovs.18-25861

59. Miyawaki A, Llopis J, Heim R, et al. Fluorescent indicators for Ca2+ based on green fluorescent proteins and calmodulin. *Nature*. 1997;388(6645):882-887. doi:10.1038/42264

60. Ye L, Haroon MA, Salinas A, Paukert M. Comparison of GCaMP3 and GCaMP6f for studying astrocyte Ca2+ dynamics in the awake mouse brain. *PLoS One*. 2017;12(7):1-17. doi:10.1371/journal.pone.0181113

61. Weitz AC, Behrend MR, Lee NS, et al. Imaging the response of the retina to electrical stimulation with genetically encoded calcium indicators. *J Neurophysiol*. 2013;109(7):1979-1988. doi:10.1152/jn.00852.2012

62. Akerboom J, Chen TW, Wardill TJ, et al. Optimization of a GCaMP calcium indicator for neural activity imaging. *J Neurosci*. 2012;32(40):13819-13840. doi:10.1523/JNEUROSCI.2601-12.2012

63. Nakai J, Ohkura M, Imoto K. A high signal-to-noise ca2+ probe composed of a single

green fluorescent protein. *Nat Biotechnol*. 2001;19(2):137-141. doi:10.1038/84397

64. Blandford SN, Hooper ML, Yabana T, Chauhan BC, Baldridge WH, Farrell SRM. Retinal characterization of the thy1-GcaMP3 transgenic mouse line after optic nerve transection. *Investig Ophthalmol Vis Sci*. 2019;60(1):183-191. doi:10.1167/iovs.18-25861

65. Biswas S, Haselier C, Mataruga A, Thumann G, Walter P, Müller F. Pharmacological analysis of intrinsic neuronal oscillations in rd10 retina. *PLoS One*. 2014;9(6). doi:10.1371/journal.pone.0099075

66. Ye JH, Goo YS. The slow wave component of retinal activity in rd/rd mice recorded with a multi-electrode array. *Physiol Meas*. 2007;28(9):1079-1088. doi:10.1088/0967-3334/28/9/009

67. Jazayeri MH, Amani H, Pourfatollah AA, Pazoki-Toroudi H, Sedighimoghaddam B. Various methods of gold nanoparticles (GNPs) conjugation to antibodies. *Sens Bio-Sensing Res*. 2016;9:17-22. doi:10.1016/j.sbsr.2016.04.002

68. Milde F, Lauw S, Koumoutsakos P, Iruela-Arispe ML. The mouse retina in 3D: Quantification of vascular growth and remodeling. *Integr Biol (United Kingdom)*. 2013;5(12):1426-1438. doi:10.1039/c3ib40085a

69. Wan J, Wang JH, Liu T, Xie Z, Yu XF, Li W. Surface chemistry but not aspect ratio mediates the biological toxicity of gold nanorods in vitro and in vivo. *Sci Rep*. 2015;5(May):1-16. doi:10.1038/srep11398

70. Li Z, Tang S, Wang B, et al. Metabolizable Small Gold Nanorods: Size-dependent Cytotoxicity, Cell Uptake and In Vivo Biodistribution. *ACS Biomater Sci Eng*. 2016;2(5):789-797. doi:10.1021/acsbiomaterials.5b00538

71. Bartneck M, Ritz T, Keul HA, et al. Peptide-functionalized gold nanorods increase liver injury in hepatitis. *ACS Nano*. 2012;6(10):8767-8777. doi:10.1021/nn302502u

72. Alkilany AM, Murphy CJ. Toxicity and cellular uptake of gold nanoparticles: What we have learned so far? *J Nanoparticle Res*. 2010;12(7):2313-2333. doi:10.1007/s11051-010-9911-8

73. Crowell SR, Wang K, Famili A, et al. Influence of charge, hydrophobicity, and size on vitreous pharmacokinetics of large molecules. *Transl Vis Sci Technol*. 2019;8(6). doi:10.1167/tvst.8.6.1

74. Jo DH, Kim JH, Lee TG, Kim JH. Size, surface charge, and shape determine therapeutic effects of nanoparticles on brain and retinal diseases. *Nanomedicine Nanotechnology, Biol Med*. 2015;11(7):1603-1611. doi:10.1016/j.nano.2015.04.015

75. Carvalho-de-Souza JL, Treger JS, Dang B, Kent SBH, Pepperberg DR, Bezanilla F. Photosensitivity of neurons enabled by cell-targeted gold nanoparticles. *Neuron*. 2015;86(1):207-217. doi:10.1016/j.neuron.2015.02.033